Physics in Medicine & Biology

PAPER • **OPEN ACCESS**

Integrated-mode proton radiography with 2D lateral projections

To cite this article: Mikaël Simard *et al* 2024 *Phys. Med. Biol.* **69** 054001

IOP Publishing Phys. Med. Biol. 69 (2024) 054001 https://doi.org/10.1088/1361-6560/ad209d

Physics in Medicine & Biology

IPEM Institute of Physics and Engineering in Medicine

OPEN ACCESS

RECEIVED
27 March 2023

REVISED
8 January 2024

ACCEPTED FOR PUBLICATION
19 January 2024

PUBLISHED
27 February 2024

PAPER

Integrated-mode proton radiography with 2D lateral projections

Mikaël Simard[1], Daniel G Robertson[2], Ryan Fullarton[1], Gary Royle[1], Sam Beddar[3] and Charles-Antoine Collins-Fekete[1]

[1] Department of Medical Physics and Biomedical Engineering, University College London, London, United Kingdom
[2] Division of Medical Physics, Department of Radiation Oncology, Mayo Clinic Arizona, 5881 E Mayo Blvd, Phoenix, AZ, United States of America
[3] The University of Texas MD Anderson UTHealth Graduate School of Biomedical Sciences, Houston, TX, United States of America

E-mail: m.simard@ucl.ac.uk

Keywords: proton imaging, proton radiography, integrated mode, proton therapy, image-guided radiotherapy

Abstract

Integrated-mode proton radiography leading to water equivalent thickness (WET) maps is an avenue of interest for motion management, patient positioning, and *in vivo* range verification. Radiographs can be obtained using a pencil beam scanning setup with a large 3D monolithic scintillator coupled with optical cameras. Established reconstruction methods either (1) involve a camera at the distal end of the scintillator, or (2) use a lateral view camera as a range telescope. Both approaches lead to limited image quality. The purpose of this work is to propose a third, novel reconstruction framework that exploits the 2D information provided by two lateral view cameras, to improve image quality achievable using lateral views. The three methods are first compared in a simulated Geant4 Monte Carlo framework using an extended cardiac torso (XCAT) phantom and a slanted edge. The proposed method with 2D lateral views is also compared with the range telescope approach using experimental data acquired with a plastic volumetric scintillator. Scanned phantoms include a Las Vegas (contrast), 9 tissue-substitute inserts (WET accuracy), and a paediatric head phantom. Resolution increases from 0.24 (distal) to 0.33 lp mm^{-1} (proposed method) on the simulated slanted edge phantom, and the mean absolute error on WET maps of the XCAT phantom is reduced from 3.4 to 2.7 mm with the same methods. Experimental data from the proposed 2D lateral views indicate a 36% increase in contrast relative to the range telescope method. High WET accuracy is obtained, with a mean absolute error of 0.4 mm over 9 inserts. Results are presented for various pencil beam spacing ranging from 2 to 6 mm. This work illustrates that high quality proton radiographs can be obtained with clinical beam settings and the proposed reconstruction framework with 2D lateral views, with potential applications in adaptive proton therapy.

1. Introduction

Proton computed tomography is a developing imaging modality that estimates the spatial distribution of the relative proton stopping power (RSP) using tomographic principles. Alternatively, radiographic images representing the water equivalent thickness (WET) of traversed tissues can be acquired. Proton imaging may be helpful for accurate treatment planning in proton therapy by limiting uncertainties in RSP estimation (Schneider and Pedroni 1995, Schaffner and Pedroni 1998, Schneider *et al* 2005, Paganetti 2012, Yang *et al* 2012, Dedes *et al* 2022). Furthermore, as the treatment and imaging sources are the same, proton imaging creates images that are fully registered with the treatment beam, and enables a direct measurement of the residual proton range in the treatment room, right before delivery. As such, proton imaging may also be useful for patient positioning and adaptive proton therapy (Parodi 2020). Specific use of proton radiographs for adaptive proton therapy include identifying the time for adaptive re-planning in head and neck cancer patients (Fukumitsu *et al* 2014, Wu *et al* 2017, Evans *et al* 2020, Meijers *et al* 2021), or rapid radiographic imaging of moving tumours towards online adaptive radiotherapy (Steinsberger *et al* 2022).

Single-event proton imaging (Johnson 2017) is the most promising approach in terms of spatial resolution and WET/RSP accuracy (Krah *et al* 2018b, Parodi 2020), although practically such systems are hindered by their high costs, slow imaging time and limited compatibility with proton fluxes commissioned for clinical systems (Parodi 2020). Integrated mode imaging, which considers the integrated signal from individual pencil beams (PB) rather than single protons, is a faster alternative generally compatible with clinical systems. While multiple integrated-mode detection systems have been proposed (Zygmanski *et al* 2000, Testa *et al* 2013, Rinaldi *et al* 2014, Farace *et al* 2016, Darne *et al* 2017, 2019, Meijers *et al* 2021, Tendler *et al* 2021, Darne *et al* 2022, Schnürle *et al* 2023), their image quality remains limited compared to single event imaging, mostly due to multiple Coulomb scattering (MCS) blurring the integrated signal, and range mixing effects. Improving image quality for integrated mode imaging therefore necessitates advanced image reconstruction techniques (Parodi 2020). While there have been some efforts to enhance image quality via deep learning models (Heyden *et al* 2021), this work explores the use of a novel physics-based reconstruction model to refine image quality.

More specifically, the purpose of this work is to present a novel proton radiography reconstruction algorithm for a fast, low-cost integrated-mode proton imaging device. The device is based on a volumetric plastic scintillator that creates a 3D light emission distribution from the dose distribution of individual PBs inside the scintillation detector. 2D projections of this signal are captured using optical apparatus such as CCD cameras (Darne *et al* 2017, 2019, Tendler *et al* 2021). The conventional setup (Tanaka *et al* 2016, Darne *et al* 2017, Tanaka *et al* 2018, Darne *et al* 2019) typically uses one CCD camera at the distal end of the scintillator, which integrates the optical signal along the beam's axis. This beam's eye view signal allows fast and straightforward reconstructions, but image quality largely suffers from MCS, and the approach requires an extensive calibration procedure to be quantitative (Darne *et al* 2019).

The setup can however be used as a range telescope, provided that the CCD camera is oriented to capture a lateral projection perpendicular to the beam's propagation axis; an early investigation has shown promise towards improved image quality (Tendler *et al* 2021). However, in that approach, the lateral projections did not exploit the beam's spatial position, which could be inferred as lateral projections result in 2D images of the Bragg curve. In addition, there was no consideration of the impact from MCS in the reconstruction process. This limits the reconstruction accuracy and does not fully take advantage of the information present in each 2D image. This study presents a reconstruction algorithm tailored specifically for the problem of WET reconstruction from a set of 2D orthogonal lateral projections which incorporates MCS physics into the reprojection, and considers range mixing effects.

A probabilistic framework for image reconstruction is first presented. Reconstructed radiographs from Monte Carlo simulations on an extended cardiac torso (XCAT) phantom as well as a slanted edge phantom are first reported to illustrate differences in image quality and WET accuracy between the proposed integrated mode method as well as conventional integrated mode distal and lateral views. Integrated mode approaches are also compared with single event proton imaging. Experimental data to reconstruct proton radiographs was also gathered for a contrast phantom (Las Vegas), 9 tissue-equivalent inserts for WET accuracy, and a paediatric head phantom for general image quality.

2. Methods

2.1. Pencil beam propagation and detection

2.1.1. Imaging setup

A pencil beam (PB) scanning setup is considered for proton imaging. Let i be the index noting individual pencil beams PB_i, with $i \in [1, N_{\mathrm{PB}}]$. Each PB_i originates at a central position $\mathbf{r}_i = (x_i, y_i, z_i)$ and propagates towards the z direction, with initial angle $\boldsymbol{\theta}_i = (\theta_{x,i}, \theta_{y,i}, \theta_{z,i}) = (\pi/2, \pi/2, 0)$. Each PB is assumed Gaussian, and has the same initial spatial and angular spread in the lateral directions x and y, defined in the covariance matrix:

$$\boldsymbol{\Sigma}_y(z_i) \equiv \boldsymbol{\Sigma}_x(z_i) = \begin{bmatrix} \sigma_x^2(z_i) & \sigma_{x\theta_x}(z_i) \\ \sigma_{x\theta_x}(z_i) & \sigma_{\theta_x}^2(z_i) \end{bmatrix}. \tag{1}$$

In the x direction, the initial spatial spread of the beam is $\sigma_x(z_i)$. The initial angular spread $\sigma_{\theta_x}(z_i)$ is the mean square angular deflection of the beam in x, and the spatial-angular covariance $\sigma_{x,\theta_x}(z_i)$ is typically obtained from a beam's measured emittance (Gottschalk 2012). For proton radiography, the aim is to reconstruct the WET of the object. The reconstruction grid has isotropic voxels of side $2\delta_k$ and the position of pixels on the grid are noted with $\mathbf{r}_k = (x_k, y_k, z_k)$,where z_k is defined from the distance between the source and the object's entrance, z_O.

$\mathbf{r}_d = (x_d, y_d, z_d)$ is the location of a detection element, with z_d defined with respect to the detector entrance, which is at distance z_D from z_i. The detector considered in this work produces a 2D signal. Figure 1 schematizes the imaging setup for a single PB, while the detection geometry is further detailed in figure 2.

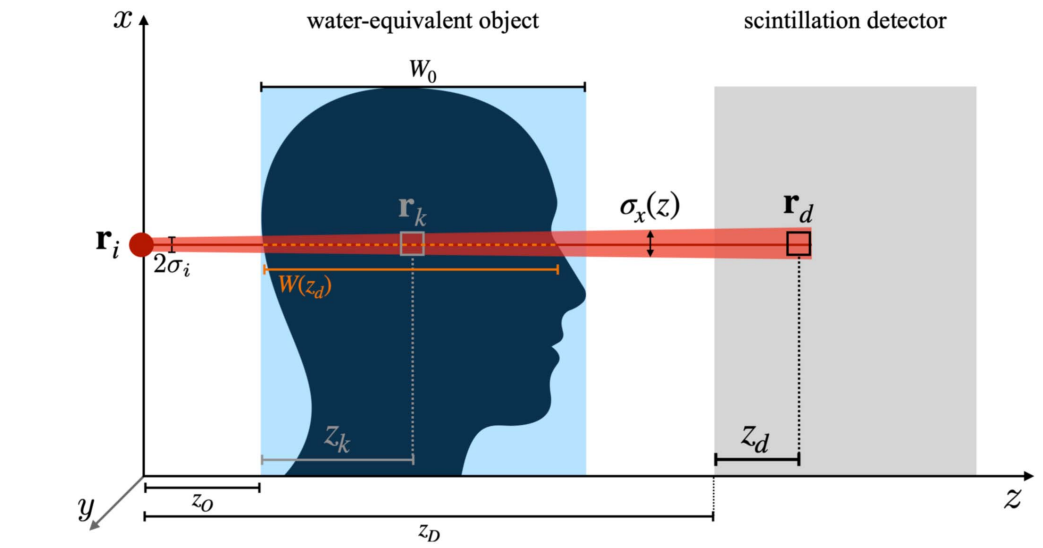

Figure 1. XZ projection of the PB scanning setup. The PB propagates z_O cm in air before traversing a WET $W(z_d)$ within the object. An additional distance (calculable using z_D) is traveled in air before energy is deposited at depth z_d in the detector. Details on how the hull of the object is considered are given in appendix B.

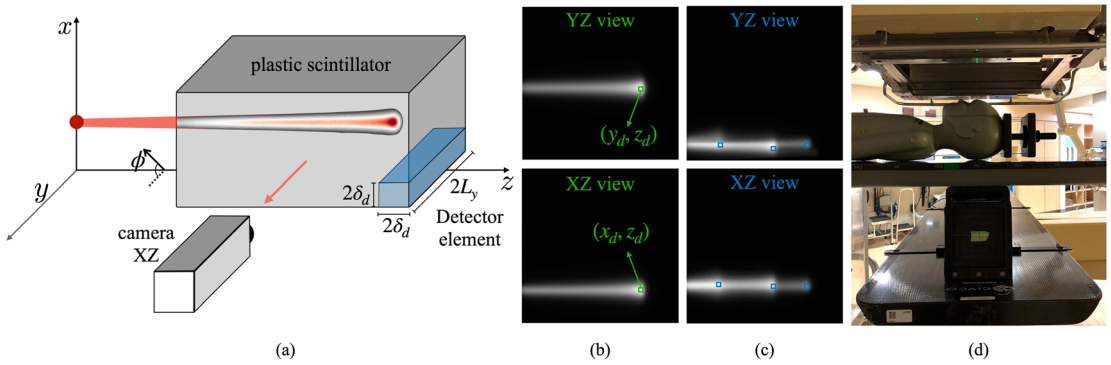

Figure 2. (a) Scintillation detector setup illustrated without an object resulting in a 2D detection system. The camera captures a XZ projection (at camera angle $\phi = 0$) of the 3D energy deposition profile, resulting in the detection element shown in the bottom right corner of the scintillator. (b) Examples of projections with the top (YZ) and lateral (XZ) views, where the central pixel of the 2D Bragg curve representing the 80% distal fall-off is identified in green in each plot. (c) Additional example illustrating a case where the pencil beam crosses structures (not shown in the figure) with different WET and result in multiple peaks. (d) photograph of a proton radiography experimental setup; see section 2.4.2 for details.

A 2D detector system is considered in this work, following the setup of Darne *et al* (2022). The setup involves a monolithic scintillator scoring 3D energy deposition. A CCD camera or any pixelised optical detector whose field of view covers the entire scintillator is positioned at angle ϕ to gather 2D projections of the 3D signal from the scintillator. In this work, images are acquired in two perpendicular lateral (XZ and YZ) planes, resulting in data acquired respectively at camera angles $\phi = 0$ and $\pi/2$. Figure 2 shows the imaging setup for the XZ projection, examples of 2D datasets for the XZ and YZ views, and an example of experimental setup.

2.1.2. Probabilistic framework

Each PB_i generates a signal in the detector at various locations $\mathbf{r}_d$. To construct a WET map, the signal at relevant detector voxels $\mathbf{r}_d$ is reprojected towards the reconstruction grid, as detailed in section 2.3. Reprojection requires the calculation of $\mathcal{P}_\phi(\mathbf{r}_k|\mathbf{r}_i,\ \mathbf{r}_d)$, the likelihood that a PB originating from $\mathbf{r}_i$ and detected at $\mathbf{r}_d$ (with a detection setup using camera angle ϕ) crosses voxel $\mathbf{r}_k$:

$$\mathcal{P}_\phi(\mathbf{r}_k|\mathbf{r}_i,\ \mathbf{r}_d) = \frac{\mathcal{P}(\mathbf{r}_k|\mathbf{r}_i)\,\mathcal{P}_\phi(\mathbf{r}_d|\mathbf{r}_k,\ \mathbf{r}_i)}{\mathcal{P}_\phi(\mathbf{r}_d|\mathbf{r}_i)}. \tag{2}$$

The right hand side includes $\mathcal{P}(\mathbf{r}_k|\mathbf{r}_i)$, the probability that the PB crosses voxel $\mathbf{r}_k$ given that it originates from $\mathbf{r}_i$. $\mathcal{P}_\phi(\mathbf{r}_d|\mathbf{r}_i)$ is defined similarly for detector location $\mathbf{r}_d$, and camera angle ϕ. $\mathcal{P}_\phi(\mathbf{r}_d|\mathbf{r}_k,\ \mathbf{r}_i)$ is the probability that the PB is

detected at $\mathbf{r}_d$ in the detector (using camera angle ϕ) knowing that it originates at $\mathbf{r}_i$ and passes through the reconstruction voxel located at $\mathbf{r}_k$.

2.2. Likelihood model based on multiple scattering theory

Relevant results from the Fermi–Eyges theory of multiple scattering (Fermi 1940, Eyges 1948) are first summarized in appendix A. Expressions for $\mathcal{P}(\mathbf{r}_k|\mathbf{r}_i)$, $\mathcal{P}_\phi(\mathbf{r}_d|\mathbf{r}_i)$ and $\mathcal{P}_\phi(\mathbf{r}_d|\mathbf{r}_k,\ \mathbf{r}_i)$ are respectively derived in sections 2.2.1, 2.2.2 and 2.2.3.

2.2.1. Transport from the source to the object

$\mathcal{P}(\mathbf{r}_k|\mathbf{r}_i)$, the likelihood that PB_i originating from $\mathbf{r}_i$ crosses a reconstruction grid voxel at $\mathbf{r}_k$, is obtained by marginalizing the beam's 3D localisation probability density function (PDF), $p(\mathbf{r}|\mathbf{r}_i)$, over the reconstruction voxel's dimensions:

$$\mathcal{P}(\mathbf{r}_k|\mathbf{r}_i) = \int_{z_k-\delta_k}^{z_k+\delta_k}\int_{y_k-\delta_k}^{y_k+\delta_k}\int_{x_k-\delta_k}^{x_k+\delta_k} p(\mathbf{r}|\mathbf{r}_i)\mathrm{d}x\mathrm{d}y\mathrm{d}z = \frac{1}{4}\left(\mathrm{erf}\left(\frac{x_k - x_i + \delta_k}{\sigma_l(z_k)}\right) - \mathrm{erf}\left(\frac{x_k - x_i - \delta_k}{\sigma_l(z_k)}\right)\right) \times \left(\mathrm{erf}\left(\frac{y_k - y_i + \delta_k}{\sigma_l(z_k)}\right) - \mathrm{erf}\left(\frac{y_k - y_i - \delta_k}{\sigma_l(z_k)}\right)\right). \tag{3}$$

$p(\mathbf{r}|\mathbf{r}_i)$ is defined in equation (A2). For the integral over z, $\sigma_l(z_k)$ is assumed constant within a given voxel (Rescigno *et al* 2015). The calculation of $\sigma_l(z_k)$, the spatial spread of the beam after propagating from z_i to z_k, is detailed in appendix B.1.

2.2.2. Transport from the source to the detector

$\mathcal{P}_\phi(\mathbf{r}_d|\mathbf{r}_i)$ is obtained by integrating $p(\mathbf{r}|\mathbf{r}_i)$ over relevant detector dimensions, which could be 1D (range telescope), 2D (this work) or 3D (voxelised detector). Considering the 2D XZ projection illustrated in figure 2, the likelihood is

$$\mathcal{P}_{\phi=0}(\mathbf{r}_d|\mathbf{r}_i) = \int_{z_d-\delta_d}^{z_d+\delta_d}\int_{-L_y}^{L_y}\int_{x_d-\delta_d}^{x_d+\delta_d} p(\mathbf{r}|\mathbf{r}_i)\mathrm{d}x\mathrm{d}y\mathrm{d}z = \frac{1}{2}\left(\mathrm{erf}\left(\frac{x_d - x_i + \delta_d}{\sigma_l(z_d)}\right) - \mathrm{erf}\left(\frac{x_d - x_i - \delta_d}{\sigma_l(z_d)}\right)\right). \tag{4}$$

In the YZ plane, $\mathcal{P}_{\phi=\frac{\pi}{2}}(\mathbf{r}_d|\mathbf{r}_i)$ is similar to equation (4), but with y_d and y_i instead of x_d and x_i. $\sigma_l(z_d)$ is the spread of the beam from z_i to z_d in the detector, and its calculation is detailed in appendix B.2.

2.2.3. Transport from the object to the detector

$\mathcal{P}_\phi(\mathbf{r}_d|\mathbf{r}_i,\ \mathbf{r}_k)$ is obtained in four steps. First, $p(\mathbf{X},\ z|\mathbf{r}_i,\ \mathbf{r}_k)$, the spatio-angular conditional PDF of protons in the XZ plane, is derived; this PDF is first introduced in equation (A1). Second, this distribution is marginalized over all angles θ_x to obtain the location conditional PDF $p(x,\ z|\mathbf{r}_i,\ \mathbf{r}_k)$. A similar procedure is performed for the y coordinate to obtain $p(y,\ z|\mathbf{r}_i,\ \mathbf{r}_k)$, and both lateral PDFs are multiplied to obtain, as a third step, the location conditional PDF $p(\mathbf{r}|\mathbf{r}_k,\ \mathbf{r}_i)$ (Jette *et al* 1983). Fourth, $\mathcal{P}_\phi(\mathbf{r}_d|\mathbf{r}_k,\ \mathbf{r}_i)$ is obtained by marginalizing $p(\mathbf{r}|\mathbf{r}_i,\ \mathbf{r}_k)$ over the detector's dimensions.

$p(\mathbf{X},\ z|\mathbf{r}_i,\ \mathbf{r}_k)$ is interpreted as the spatio-angular PDF of a PB coming from $\mathbf{r}_i$ and passes through the voxel at location $\mathbf{r}_k$. The condition of passing through $\mathbf{r}_k$ is viewed as the beam being collimated by a virtual 2D collimator at the reconstruction voxel's location between lateral coordinates $[x_k - \delta_k,\ x_k + \delta_k]$ and $[y_k - \delta_k,\ y_k + \delta_k]$ at depth $z = z_k$. The calculation of the location PDF for a collimated PB is based on the Fermi–Eyges PB summation method, whose details can be found in the work of Sabbas *et al* (1987) and Safai *et al* (2008):

$$p(\mathbf{X},\ z|\mathbf{r}_i,\ \mathbf{r}_k) = \int_{\mathrm{coll.}}\int_{-\infty}^{\infty} p_{\mathrm{FE}}(\mathbf{X},\ z|\mathbf{X}',\ z_k)\ \alpha(x',\ \theta_x',\ z_k)\ \mathrm{d}\theta_x'\mathrm{d}x'. \tag{5}$$

Here x' and θ_x' are integration variables denoting the position and angle of protons at the collimator plane. $p_{\mathrm{FE}}(\mathbf{X},\ z|\mathbf{X}',\ z_k)$ is the PDF of a needle-like Gaussian beam propagating from z_k to z, which assumes initial values of $\mathbf{\Sigma}_x(z_k) = 0$, and is calculated with equation (A1). $\alpha(x',\ \theta_x',\ z_k) \equiv p_{\mathrm{FE}}(\mathbf{X}',\ z_k|\mathbf{X}_i,\ z_i)$ is the distribution of protons at the collimator plane, also obtained with equation (A1), with elements of $\mathbf{\Sigma}_x(z)$ calculated in the same way as in section 2.2.1. Furthermore, integration over the collimator dimensions in x' (coll.) is from $x_k - \delta_k$ to $x_k + \delta_k$.

The intermediate result for $p(\mathbf{X},\ z|\mathbf{r}_i,\ \mathbf{r}_k)$ is not shown for brevity; $p(x,\ z|\mathbf{r}_k,\ \mathbf{r}_i)$ is obtained after marginalizing $p(\mathbf{X},\ z|\mathbf{r}_i,\ \mathbf{r}_k)$ over all angles θ_x:

$$p(x,\ z|\mathbf{r}_i,\ \mathbf{r}_k) = \frac{1}{N_x\sqrt{\pi\kappa}}\exp\left(-\frac{(x-x_i)^2}{\kappa}\right)\left[\mathrm{erf}\left(\frac{\kappa_2(x - x_k + \delta_k) + \kappa_1(x_i - x_k + \delta_k)}{\sqrt{\Delta\kappa}}\right) - \mathrm{erf}\left(\frac{\kappa_2(x - x_k - \delta_k) + \kappa_1(x_i - x_k - \delta_k)}{\sqrt{\Delta\kappa}}\right)\right]. \tag{6}$$

In equation (6), N_x is a normalization constant to obtain probabilities, and the following variables are introduced:

$$\begin{cases} \kappa_1 = \mathcal{A}_2(z) + \sigma_{x\theta_x}(z_k)\cdot(z-z_k) + \sigma^2_{\theta_x}(z_k)\cdot(z-z_k)^2 \\ \kappa_2 = \sigma^2_x(z_k) + \sigma_{x\theta_x}(z_k)\cdot(z-z_k) \\ \kappa = \kappa_1 + \kappa_2 \\ \Delta = \sigma^2_x(z_k)\cdot\kappa_1 - \sigma_{x\theta_x}(z_k)\cdot(z-z_k)\cdot\kappa_2 \end{cases}. \tag{7}$$

Here, the elements of the covariance matrix $\sigma_*(z_k)$ are obtained after propagation from z_i to the object voxel's location z_k, and $\mathcal{A}_2(z)$ is the multiple scattering contribution to spatial spread (equation (A6)) from the object voxel's location z_k to an arbitrary depth z. Details to calculate $\sigma_*(z_k)$ and $\mathcal{A}_2(z)$ are provided in appendix B.3.

The joint PDF $p(\mathbf{r}|\mathbf{r}_i,\ \mathbf{r}_k)$ is obtained as the product of $p(x,\ z|\mathbf{r}_i,\ \mathbf{r}_k)$ and $p(y,\ z|\mathbf{r}_i,\ \mathbf{r}_k)$ but is not shown for brevity. From $p(\mathbf{r}|\mathbf{r}_i,\ \mathbf{r}_k)$, the likelihood $\mathcal{P}_\phi(\mathbf{r}_d|\mathbf{r}_i,\ \mathbf{r}_k)$ is obtained by integrating over the detector dimensions. Using the example of the 2D XZ projection shown in figure 2, one obtains

$$\mathcal{P}_{\phi=0}(\mathbf{r}_d|\mathbf{r}_i,\ \mathbf{r}_k) = \int_{z_d-\delta_d}^{z_d+\delta_d}\int_{-L_y}^{L_y}\int_{x_d-\delta_d}^{x_d+\delta_d} p(\mathbf{r}|\mathbf{r}_i,\ \mathbf{r}_k)\,\mathrm{d}x\mathrm{d}y\mathrm{d}z \approx \int_{x_d-\delta_d}^{x_d+\delta_d} p(x,\ z_d|\mathbf{r}_i,\ \mathbf{r}_k)\,\mathrm{d}x. \tag{8}$$

The integral over y equals 1, as it is assumed that the y component of $p(\mathbf{r}|\mathbf{r}_i,\ \mathbf{r}_k)$ is fully contained within the detector. As there is no analytical solution to equation (8), $\mathcal{P}_{\phi=0}(\mathbf{r}_d|\mathbf{r}_i,\ \mathbf{r}_k)$ is obtained through numerical integration.

2.3. Reprojection from joint lateral views

2.3.1. Joint likelihood

Consider the specific case where two lateral views with camera angles $\phi = 0$ and $\phi = \pi/2$ (XZ and YZ planes) are obtained. Assuming that each 2D image is composed of one or more identifiable Bragg peaks that can be associated with various structures traversed by the beam, it is possible to match signals from both 2D views and infer the 3D position of the Bragg peaks. In other words, the $(x_d,\ z_d)$ positions from the XZ view and $(y_d,\ z_d)$ positions from the YZ views shown in figure 2 are combined to obtain $\mathbf{r}_d = (x_d,\ y_d,\ z_d)$, where z_d is taken as the average position between the two views to account for experimental or algorithmic uncertainties. With the proposed experimental setup, the difference between the two views was found to vary by no more than one pixel. In this situation, the likelihood of equation (2) becomes the intersection of both views:

$$\mathcal{P}(\mathbf{r}_k|\mathbf{r}_i,\ \mathbf{r}_d) = \frac{\mathcal{P}(\mathbf{r}_k|\mathbf{r}_i)\mathcal{P}_{\phi=0}(\mathbf{r}_d|\mathbf{r}_k,\ \mathbf{r}_i)\mathcal{P}_{\phi=\pi/2}(\mathbf{r}_d|\mathbf{r}_k,\ \mathbf{r}_i)}{\mathcal{P}_{\phi=0}(\mathbf{r}_d|\mathbf{r}_i)\mathcal{P}_{\phi=\pi/2}(\mathbf{r}_d|\mathbf{r}_i)}. \tag{9}$$

Equation (9) can be obtained by considering the derivations of section 2.2 with a 3D detector element instead.

2.3.2. Reprojection equation

For a given detection geometry, each PB_i generates a signal $S_i(\mathbf{r}_d)$ at multiple $\mathbf{r}_d$. Projection data can be generated similarly to the distance-driven binning procedure suggested by Rescigno *et al* (2015), which is an adaptation of Rit *et al*'s distance-driven binning framework (Rit *et al* 2013). The WET value for reconstruction voxel $\mathbf{r}_k$, $g(\mathbf{r}_k)$, is the weighted sum, over all pencil beams and relevant detector locations, of the WET associated with each location $\mathbf{r}_d$,$W(z_d)$:

$$g_\phi(\mathbf{r}_k) = \frac{\sum_{i=1}^{I_p}\sum_d \mathcal{P}(\mathbf{r}_k|\mathbf{r}_i,\ \mathbf{r}_d)\,W(z_d)}{\sum_{i=1}^{I_p}\sum_d \mathcal{P}(\mathbf{r}_k|\mathbf{r}_i,\ \mathbf{r}_d)}. \tag{10}$$

$\mathcal{P}(\mathbf{r}_k|\mathbf{r}_i,\ \mathbf{r}_d)$ is the joint likelihood of equation (9), and $W(z_d)$ is obtained from the depth z_d of the detector pixel:

$$W(z_d) = W_0 - z_d\,\mathrm{RSP}_{\mathrm{det}}, \tag{11}$$

with W_0 the WET of the PB and $\mathrm{RSP}_{\mathrm{det}}$ is the RSP of the detector. Equation (10) includes a summation over all relevant detector locations. In the simple case of figure 2(b), a single pixel is used; in the case of figure 2(c), where multiple structures of different WET are in the way of the beam, the three peaks should be identified and a single pixel reprojected for each. To identify peaks, the 2D signal is integrated over the x or y axis to generate an integral depth dose profile. A peak finding routine (Du *et al* 2006) is applied to find the z position(s) of candidate peaks, and the corresponding lateral (x_d or y_d) central position of each peak is obtained from the pixel with the maximum intensity in the lateral profile in the vicinity of the z position. Then, the depth to reproject, z_d, is estimated by taking the pixel in the IDD with the 80% distal intensity fall-off from the integral depth dose profile. The 3D position is then obtained by matching the peaks of both lateral views (XZ and YZ) according to the distance between their coordinates z_d.

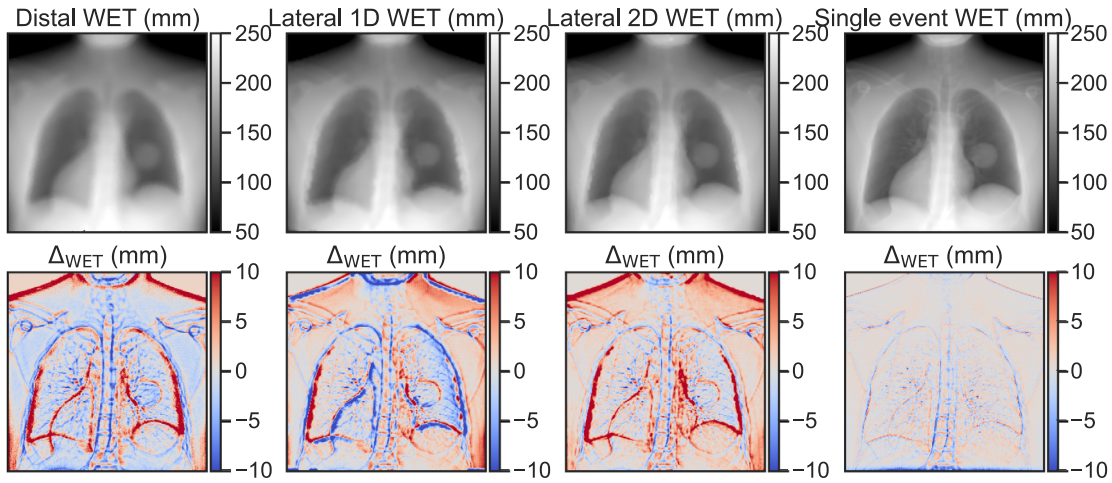

Figure 3. WET maps (top) and absolute error Δ_{WET} (bottom) in mm of the simulated XCAT phantom using a 3 mm beam spacing, for the four reconstruction methods (left to right). Lateral 2D is the proposed approach of this work.

2.4. Data production

2.4.1. Monte Carlo simulations

Monte Carlo simulations were performed with the Geant4 software toolkit (version 10.6) (Agostinelli 2003), using the same geometry as presented in figure 1. Detailed simulation parameters following AAPM TG-268 guidelines (Sechopoulos *et al* 2018) are the same as in table 1 of Tendler *et al* (2021), with the following differences: the source geometry consisted of two 2D Gaussian functions, the first Gaussian, containing 75% of the beam intensity, and having a spread corresponding to the spot size and the second Gaussian having a spread twice the spot size with the remaining 25% intensity. Angular spread was sampled from a Gaussian distribution characterized by a defined beam divergence. There were 4×10^6 histories per pencil beam position, which were centered on evenly distributed points across the field of view. A distance of $z_D = 40cm$ was used and the object was centered at $z_D/2$ from the beam. A $30 \times 30 \times 30$ cm^3 detector object with the density and composition of the EJ-260 plastic scintillator (Darne *et al* 2022) was used to simulate the volumetric scintillation detector and score energy, which was transformed to quenched light emission following Birks' law (Tendler *et al* 2021).

Images were acquired at an energy of 200 MeV using a spot size of $\sigma_x(z_i) = \sigma_y(z_i) = = 3$ mm, and angular divergence of $\sigma_{\theta_x}(z_i) = \sigma_{\theta_y}(z_i) = 3$ mrad. Raw data is acquired with pencil beams spaced by 1 mm. This creates a large dataset which can be sub-sampled to study the impact of beam spacing on image quality.

Two phantoms were imaged: one phase of the extended cardiac phantom (XCAT) (Segars 2010), and an aluminum cube (5 cm of side) with a slanted edge at 2.5° placed inside a 10 cm water tank. The XCAT was acquired with a 30×30 cm^2 field of view (FOV), and is reconstructed using spacings of 2–6 mm in increments of 1 mm, to evaluate the impact of beam spacing. The slanted edge was acquired using a 15×15 cm^2 FOV and reconstructed with a 3 mm spacing to report resolution with a spacing that limits imaging dose. As the FOV of the XCAT matches the size of the detector, partial signal loss was observed in some PBs at the edge of the scintillator. All algorithms where however robust to partly losing data from the Bragg curve, as illustrated in figure 3.

2.4.2. Experimental datasets

Proton radiographs were acquired at Mayo Clinic Arizona using a $15 \times 15 \times 15$ cm^3 plastic volumetric scintillator (EJ-260, Eljen Technologies, Sweetwater, TX) and a CMOS camera (PGE-23S3M-C, Teledyne FLIR, Wilsonville, OR) with a 25 mm lens (M118FM25, Tamron, Commack, NY), housed in a light-tight box made from black acrylic plastic. Projected 2D lateral views of the 3D energy deposition in the scintillator were acquired; the two lateral views (XZ and YZ planes) were obtained sequentially by rotating the couch by 90° between acquisitions. The imaging field of view was set to 13×13 cm^2. The following phantoms were scanned: Las Vegas (Tendler *et al* 2021) for contrast, 9 tissue-substitute cylindrical inserts (CIRS 062M electron density phantom, Sun Nuclear, Norfolk, VA) for WET accuracy, and a paediatric head phantom (Sun Nuclear ATOM Phantom, Model 704) for general image quality with a thicker object (>12 cm WET). The 9 tissue-substitute inserts were: lung (inhale), lung (exhale), adipose, plastic water, muscle, liver, bone 200 mg/cc, bone core 800 mg/cc, and bone 1500 mg/cc. Data was acquired using clinical settings at 135.6 MeV for all phantoms but the paediatric head, which was acquired at 189 MeV. Beam widths $\sigma_l(z)$ at isocenter are respectively 3.1 and 2.5 mm for 135 and 189 MeV. Data acquisition was done using pencil beam spacings of 2, 3, 4 and 5 mm. A sampling of 6 mm is also generated by sub-sampling the 3 mm acquisition. The experimental setup is shown in figure 2(d); the detector was set on the treatment couch, and an additional couch was inserted between the nozzle and detector

to hold phantoms. The distance from the nozzle to the top of the phantom was set to ≈20 cm, and the phantom to scintillator distance was 11 cm. Finally, the imaging dose as well as dose considerations are reported in appendix C.

Raw data from the CCD camera is corrected for multiple optical artifacts according to Robertson *et al* (2013). Briefly, images are corrected from perspective and refraction by projecting pixel intensities to the front of the detector according to geometrical and refraction principles. In addition, as the proposed image reconstruction framework assumes parallel beams, the small divergence angle of each beam is corrected by rotating the image by the negative of the divergence angle, assuming the center of rotation is the central position of the beam at $z_D = 0$. Finally, all WET values are corrected by subtracting the WET of objects in the beam's path (5 mm for the entrance window of scintillator, 8.3 mm for the couch).

2.5. Comparison with other methods

Four reconstruction methods are compared in this work, and are referred to as distal, lateral 1D, lateral 2D, and single event. The distal method is an integrated-mode imaging method that uses the beam-eye view (XZ) with the setup of figure 2 for image reconstruction. The signal is integrated along the beam's axis, and does not provide a direct measurement of the WET. However, the intensity can be mapped back to the WET by producing an energy-specific calibration curve that relates scintillator intensity to WET; the approach presented in Darne *et al* (2022) is used. To limit multiple scattering induced blur, only the pixels whose intensity is $\geqslant$ to 70% of the maximum intensity for each pencil beam image are reprojected.

The lateral 2D method is the one proposed in this study, which makes use of the two lateral views. To illustrate the benefits of the proposed lateral approach, a simpler lateral 1D method based on the work of Rescigno *et al* (2015) is also implemented. Briefly, the signal from one of the lateral views (either XZ or YZ) is summed over the lateral coordinate to produce a percent depth light curve, which reproduces a range telescope measurement. For reprojection, the approach of Rescigno *et al* (2015) is used, which is a specific case of the proposed algorithm; the reprojection equation is the same as equation (10), but the likelihood is directly $\mathcal{P}(\mathbf{r}_k|\mathbf{r}_i)$, as the detection event is assumed to have a probability of 1. The last method is a single event tracking method based on a front-tracker-binning method (Volz *et al* 2020), and is only used on the Monte Carlo data to compare the three integrated mode methods with a reference method in proton imaging. Plane tracking detectors are assumed ideal and only score primary generated particles (in Geant4, CreatorProcess 0) as an idealised particle imaging filter.

2.6. Data analysis

The XCAT is characterised in terms of WET accuracy. Absolute error maps Δ_{WET}, calculated between the ground truth XCAT WET and the reconstructed WET as well as the mean absolute error (MAE) calculated over the entire image are reported. The slanted edge phantom is used to estimate the resolution by following the methodology of Fujita *et al* (1992); the resolution is defined as the spatial frequency at which the modulation transfer function (MTF) drops to 10%. The Las Vegas phantom is composed of 28 holes with variable diameter and depth. The contrast is reported for all visible holes of the phantom, in a manually defined region of interest in the inner 50% of each hole; missing data in figure 5(c) should be interpreted as not visible holes in the resulting radiographs.

The contrast C is defined as $C = \frac{W_{\text{ref}} - W_{\text{min}}}{\tilde{W}}$, where W_{ref} is a reference WET value in the close vicinity of the hole, and W_{min}, $\tilde{W}$ are respectively the lowest and mean WET values in the ROI. W_{ref} was estimated manually for each hole by considering profile lines around the center of each hole and averaging the intensities on each side of the hole.

For WET accuracy, the ground truth WET of each cylindrical insert was measured using a scanning water tank and a multi-layer ionisation chamber. Estimated values from radiographs are taken as the average in a region of interest representing the inner 70% of each insert to limit edge effects. The mean absolute and relative errors over all inserts are reported, along with the standard errors on the mean (SEM). For N inserts, each with standard deviation σ_n, the SEM is defined as $\text{SEM} = \sqrt{N^{-1}\sum_{n=1}^{N}\sigma_n^2}$. Experiments described in sections 2.4–2.6 are summarised in table 1.

3. Results

Monte Carlo results are first presented in figures 3 and 4, while figures 5–7 illustrate experimental results. Finally, the impact of beam spacing is reported in figure 8, for both Monte Carlo and experimental datasets. Figure 3 compares the general image quality and WET accuracy of the proposed reconstruction method with other reference methods introduced in section 2.5 for the XCAT phantom, using a beam spacing of 3 mm to limit imaging dose and time.

The mean absolute error (MAE) in the WET images of figure 3 are 3.4 mm (distal), 3.2 mm (lateral 1D), 2.7 mm (lateral 2D) and 1.2 mm (single event). Figure 4 shows the reconstructed slanted edge also using a beam spacing of 3 mm and for the four reconstruction methods. Image resolution obtained from the MTFs are 0.24 lp mm^{-1} (distal), 0.27 lp mm^{-1} (lateral 1D), 0.33 lp mm^{-1} (lateral 2D) and 1.2 lp mm^{-1} (single event).

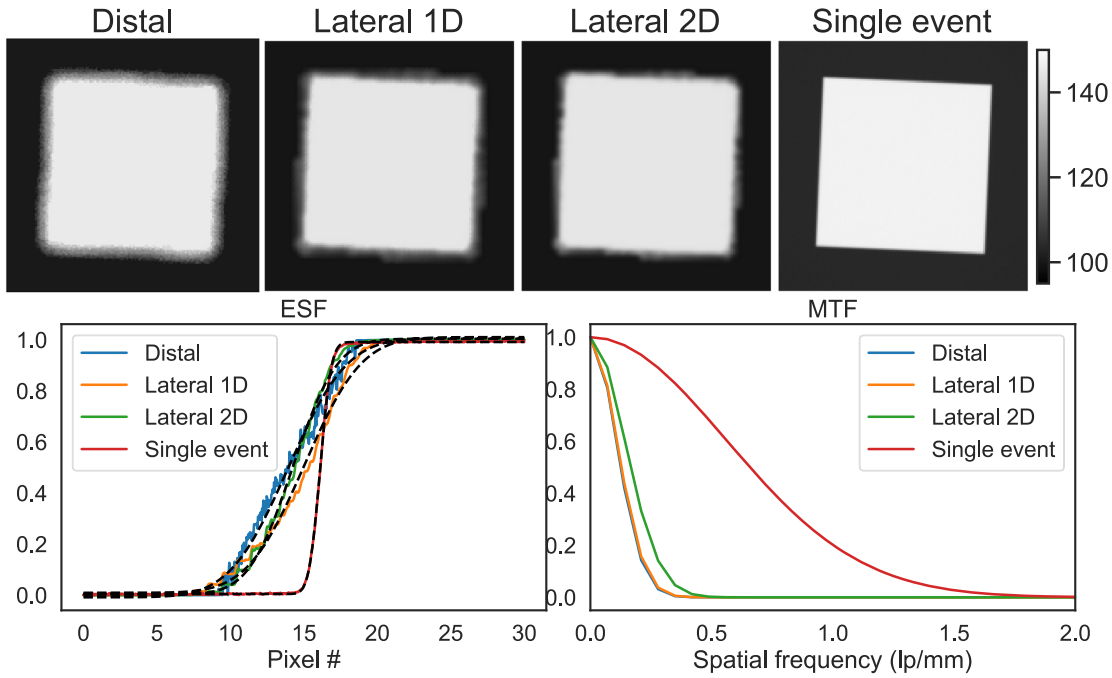

Figure 4. Top: water equivalent thickness maps (mm) of the simulated slanted edge phantom using a 3 mm beam spacing, for the four reconstruction methods (left to right). Bottom left: resulting edge spread functions (colour) and associated fit (dashed lines). Bottom right: modulation transfer functions for each method.

Table 1. List of scanned/simulated phantoms with the reconstruction methods and performance metrics used.

Phantom	Acquisition type	Reconstruction methods	Quantification metric
XCAT	Simulated	Distal, lateral 1D, lateral 2D, single event	Δ_{WET}, MAE for WET accuracy
Slanted edge	Simulated	Distal, lateral 1D, lateral 2D, single event	Spatial resolution from MTF
Las Vegas	Experimental	Lateral 1D, lateral 2D	Contrast
CIRS inserts	Experimental	Lateral 1D, lateral 2D	MAE for WET accuracy
Paediatric head	Experimental	Lateral 1D, lateral 2D	qualitative evaluation

The Las Vegas phantom is shown in figure 5, where general image quality and a quantitative analysis of contrast are reported for the lateral 1D and lateral 2D methods.

Averaged over all hole diameters and hole depths, shown in figure 5(c), the lateral 2D method provides an average relative increase in contrast by 36% compared to the lateral 1D method. Figure 6 illustrates the WET accuracy of each tissue substitute insert estimated with the lateral 2D approach proposed in this work. Averaged over the 9 inserts, the mean relative WET error is $1.2 \pm 0.3\%$, or 0.4 ± 0.1 mm in absolute. While not shown, the WET accuracy of the lateral 1D method was found to be similar, at 0.5 ± 0.1 mm.

WET maps from the proposed reconstruction method for the paediatric head phantom are shown in figure 7 for multiple beam spacings. This qualitatively illustrates the image quality that can be achieved with the current setup on a realistic geometry. Figure 8 shows, for the proposed reconstruction approach, the impact of beam spacing on reconstruction for (a) the simulated XCAT phantom and (b) the experimentally acquired Las Vegas phantom.

4. Discussions and conclusions

The results obtained in this work highlight the potential of the proposed reconstruction framework with 2D lateral projections to maximise image quality for integrated mode proton radiographs. While the distal view approach has been used for scintillation-based integrated mode detectors (Darne *et al* 2022), Monte Carlo simulations demonstrate that the distal view provides the overall lowest proton radiograph image quality compared to other views. Quantitative accuracy for the XCAT phantom as well as image resolution estimated from the slanted edge phantom are the lowest compared to all other methods evaluated. The blurriness visible in the distal WET maps of figures 3 and 4 is mainly attributed to MCS, as the integrated signal reprojected towards the imaging plane in the distal view is largely contaminated by MCS. The impact of MCS is limited for lateral views—while uncertainty due to MCS is considered to generate $\mathcal{P}(\mathbf{r}_k|\mathbf{r}_i, \mathbf{r}_d)$, the reprojected data itself is not

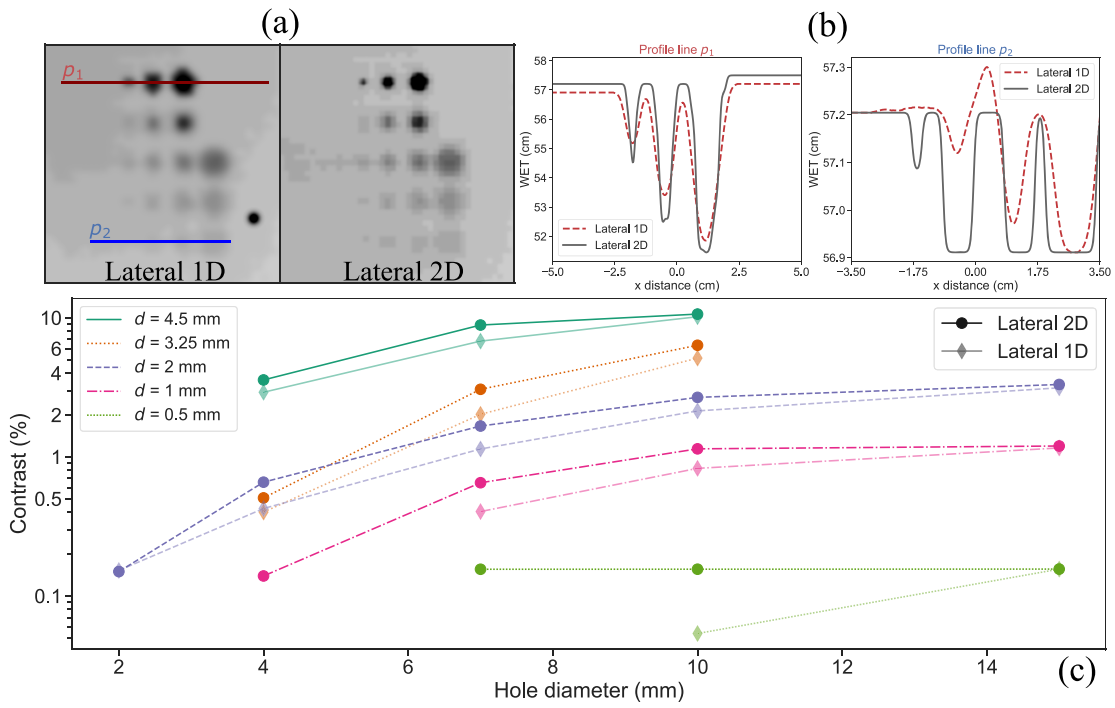

Figure 5. (a) Experimental WET maps of the Las Vegas phantom for a 3 mm beam spacing using the lateral 1D and 2D methods. The dynamic range is from 53 to 59 mm. The observed intensity dip in the lateral 1D figure (top right of profile line p_2) is due to a noisy signal from a single PB. (b) Line profiles corresponding to the p_1 and p_2 lines identified in sub-figure (a). (c) Corresponding calculated contrast for each visible inserts of the Las Vegas phantom for each reconstruction approach. Data is shown as a function of hole diameters for various hole depths d.

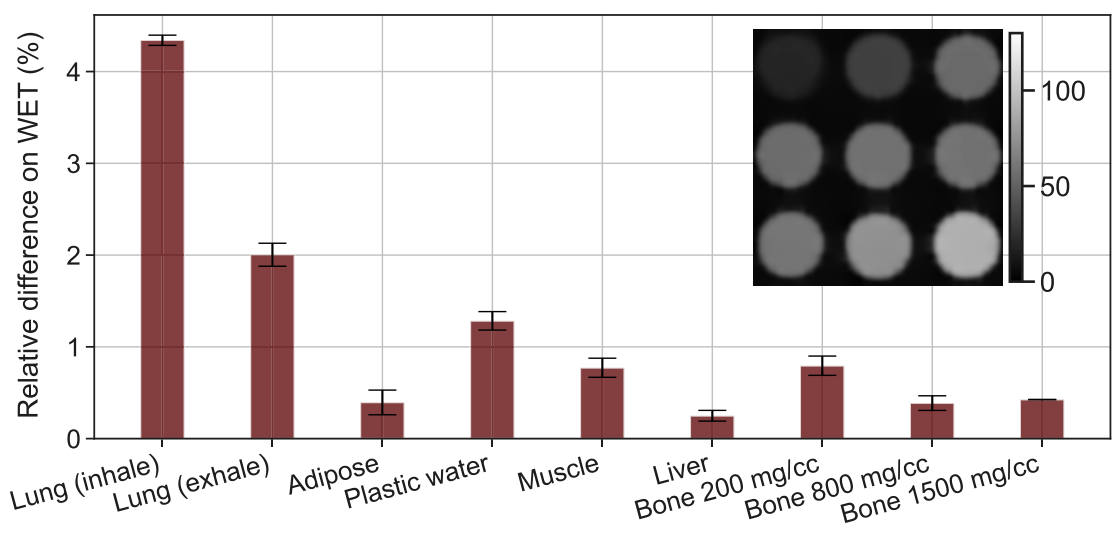

Figure 6. Experimental WET accuracy for 9 tissue substitute inserts, estimated with the proposed lateral 2D approach. Relative differences on the WET are shown along error bars representing the standard deviation inside the selected region of interest.

largely contaminated by MCS. In figure 3, it is noticeable that integrated mode methods produce more biased images than single event methods. This can be attributed to the thick, heterogeneous geometry (XCAT phantom) that result in highly complex dose distributions. While range mixing can be deconvolved in relatively simple heterogenous geometries (for instance, geometries that would produce dose distributions such as figure 2(c)), it is more difficult to manage with thick scatterers that produce a broad dose distribution. Indeed, the peak finding routine can fail in the situation where individual peaks associated with different tissues or interfaces cannot be resolved from one another.

Results highlight the clear improvements obtained with the proposed method (lateral 2D) compared to a conventional treatment for lateral data (lateral 1D). The 1D method is equivalent to a range telescope that reprojects a single WET value per PB towards the imaging plane with weights $\mathcal{P}(\mathbf{r}_k|\mathbf{r}_i)$ (equation (3)), per Rescigno *et al* (2015). The

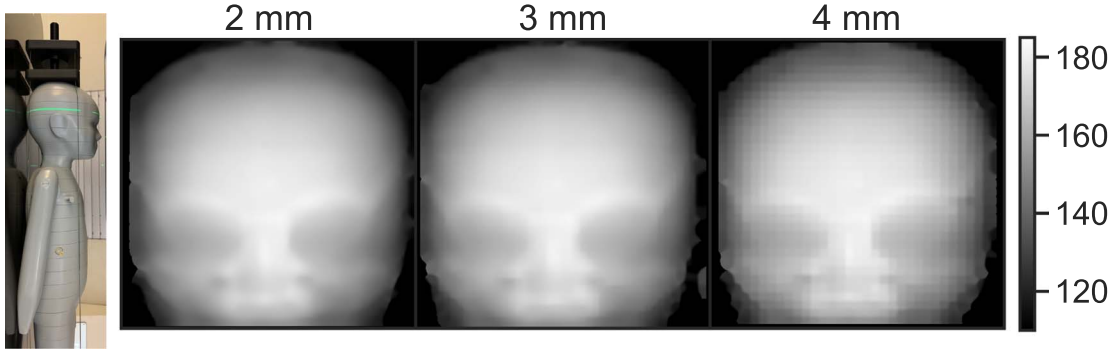

Figure 7. (Left) photograph of the paediatric head phantom, (right) experimental WET maps (mm) of the phantom reconstructed using the lateral 2D method for beam spacings of 2, 3 and 4 mm.

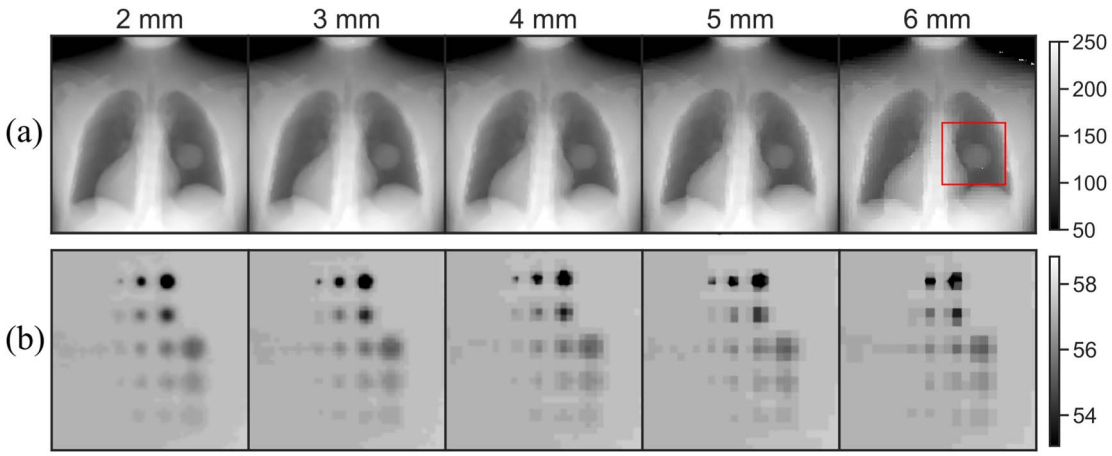

Figure 8. Water equivalent thickness maps reported as a function of beam spacing for (a) the simulated XCAT phantom and (b) the experimental Las Vegas phantom, reconstructed with the lateral 2D method. For scale, the red square in (a) represents a 10×10 cm^2 region of interest.

proposed approach can be seen as a generalisation of Rescigno *et al* to a 2D detector. In terms of WET accuracy, while it was found that the experimental WET accuracy on 9 uniform tissue inserts is similar between the lateral 1D and 2D methods (0.5 versus 0.4 mm mean error), it was also reported that the mean absolute error in WET is reduced by 15% in the simulated XCAT phantom (3.2–2.7 mm) with the lateral 2D approach. As the XCAT accuracy is calculated over the entire image, this suggests that the lateral 2D approach is better at handling heterogeneous geometries. Image resolution, calculated on the simulated slanted edge, also improves relatively by 22%. Finally, based on experimental radiographs of the Las Vegas phantom, contrast improves on average by 36%. The improvement from lateral 1D to lateral 2D is mainly attributed to two factors. First, the difference in the reprojection point spread function—namely equation (9) in the lateral 2D case, and equation (3) in the lateral 1D case. The point spread function of equation (9) has the advantage of modelling scattering inside the detector and provides a more realistic model of transport from the object to the detector. In other words, the current approach accounts for the full 3D path of the beam, whereas Rescigno *et al*'s work only considers the initial position of the beam. Second, the lateral 2D approach with both views also has the advantage of spatially localising the position of multiple Bragg peaks in a single dataset, acting similarly to a pixel detector (Krah *et al* 2018b), limiting the impact of range mixing effects.

Experimental image quality is found to be maximised with the proposed reconstruction framework. Excellent WET accuracy of 0.4 mm, calculated over 9 tissue-equivalent inserts, is obtained. This value is consistent with Krah *et al* (2018a), who have reported 0.2–0.5 mm WET error on tissue-equivalent inserts using a multi-layer ionisation chamber (Qube by De.tec.tor, Turin, Italy), and an improvement upon (Deffet *et al* 2020), which have reported 1.5mm WET accuracy with a deconvolution approach. Results also appear at least as accurate as the carbon-ion radiographs of Magallanes *et al* (2019), which reported WET relative errors below 1.3% for most of 6 tissue-equivalent slabs, although adipose and lung exceeded 3%.

An advantage of the proposed imaging framework is that high quality radiographs can be acquired and reconstructed rapidly. Oria *et al* (2023) have used a flat panel based integrated mode system combined with energy

scanning. Using 10 energies, which results in an imaging time of approximately 40 min for a 27×27 cm^2 field of view, a mean absolute WET error of approximately 5 mm is obtained in simulated datasets. In the present study, assuming an acquisition of 3 ms per pencil beam (Langner *et al* 2017), which could be obtained with the low dose measurements reported in table 2, the full 30×30 cm^2 field of view of the XCAT phantom with a 3 mm spacing can be acquired in 30 s, with a mean absolute WET error of 2.7 mm. The head phantom shown in figure 7 could be obtained in 5.5 s with a beam spacing of 3 mm. This opens applications for adaptive proton therapy in terms of patient positioning, *in vivo* range verification, and adaptive re-planning. Rapid radiographic imaging of moving tumours can also be considered—for instance, the 10×10 cm^2 square ROI identified in figure 8 with the 6 mm spacing could be acquired in 0.9 s. However, further investigations are required to explore usability for tracking purposes, as the coarse 6 mm sampling can result in distorted image features, as highlighted in figure 8(b).

This study comes with some limitations. First, the proposed approach does not simulate nor correct optical blurring that arises with scintillation-based detectors (Tendler *et al* 2021). Imaging quality obtained in silico may therefore be overestimated compared to current experimental results. Incorporating optical blurring into the proposed formalism could however lead to improved experimental image quality. Furthermore, fast imaging is conditional on (1) the use of a high-speed camera (frame rate $>$ 330 Hz (Langner *et al* 2017), which is commercially available), (2) a triggering system (either hardware based (Alsanea *et al* 2019) or software based) to synchronise image acquisition with pencil beams, and (3) a fast reconstruction framework. Due to limitations in frame rate of the current camera, experimental datasets were acquired at relatively high dose per PB to increase acquisition time per PB, which is not clinically practical. However, we have tested, with single pencil beams acquired at the doses presented in table 2, that the estimation of z_d is robust to noisy images, and we do not anticipate any problems with lower dose images (see section C). The current reconstruction time is in the tens of seconds for a 3 mm spacing, and should be improved via GPU acceleration. Future work therefore include optimising both hardware and software components to explore adaptive radiotherapy applications. Furthermore, the current detector setup (figure 2(d)) constrains the gantry angle to be at either 0 or 90 degrees (or 180 and 270), which may limit applications in treatment adaptation.

In this work, it was found that the spatial resolution estimated on the slanted edge phantom varies minimally with beam spacing, for instance ranging from 0.35 (lateral 2D, 1 mm spacing) to 0.33 lp mm^{-1} (lateral 2D, 3 mm spacing, shown in figure 4). The main improvements in resolution are obtained by modifying the image reconstruction strategy. The relationship between spatial resolution and beam spacing requires further investigation—for small objects, larger beam spacing leads to distorted images (figure 8), which can have unexpected impact on phantoms such as the slanted edge. We recommend that further investigations are performed with adequate line pair modules.

This work introduces a novel reconstruction framework for integrated-mode proton radiographs using 2D lateral views of individual pencil beams, which provides improved image quality compared to using a range telescope. High quality proton radiographs can be obtained with clinical beam settings using a fast, low-cost scintillation-based system with two cameras capturing both lateral views.

Acknowledgments

This project has received funding from the European Union's Horizon 2020 research and innovation programme under the Marie Skłodowska-Curie grant agreement No 101023220. It was also supported by the UKRI Future Leaders Fellowship, No. MR/T040785/1, the Radiation Research Unit at the Cancer Research UK City of London Centre Award C7893/A28990, and the MDACC ROSI Award. The authors also acknowledge Lennart Volz for fruitful discussions and support for Monte Carlo simulations.

Data availability statement

The data cannot be made publicly available upon publication because the cost of preparing, depositing and hosting the data would be prohibitive within the terms of this research project. The data that support the findings of this study are available upon reasonable request from the authors.

Appendix A. Fermi–Eyges multiple scattering theory

A.1. Location probability density function $p(\mathbf{r}|\mathbf{r}_i)$

The state of a PB propagating for instance in the XZ plane (for instance, in figure 2) at location $\mathbf{r}$ is described with $\mathbf{X} = (x\ \theta_x)^{\mathrm{T}}$. $\mathbf{X}_i = (x_i\ \theta_{x,i})^{\mathrm{T}}$ is similarly defined at $\mathbf{r}_i$. The depth-dependent angular-spatial probability density function (PDF) of a PB with initial state $\mathbf{X}_i$, $p_{\mathrm{E}}(\mathbf{X}, z|\mathbf{X}_i, z_i)$, is (Fermi 1940, Eyges 1948, Ibbott 1985):

$$p_{\mathrm{FE}}(\mathbf{X}, z|\mathbf{X}_i, z_i)=\frac{1}{2\pi\ |\boldsymbol{\Sigma}_{\boldsymbol{x}}(z)|^{1/2}}\exp\left(-(\mathbf{X}-\mathbf{R}_i\mathbf{X}_i)^{\mathrm{T}}\boldsymbol{\Sigma}_{\boldsymbol{x}}^{-1}(z)(\mathbf{X}-\mathbf{R}_i\mathbf{X}_i)\right), \tag{A1}$$

$\mathbf{R}_i$ is a transvection matrix whose expression can be found in prior work (Schulte *et al* 2008, Collins-Fekete *et al* 2017). A similar equation can be defined in the YZ plane, using the state variable $\mathbf{Y} = (y\ \theta_y)^{\mathrm{T}}$. Equation (A1) is independent on planes XZ and YZ. Details on how to calculate $\boldsymbol{\Sigma}_{\mathbf{x}}(z)$ are provided in section A.2. For integrated-mode imaging, the 3D location PDF $p(\mathbf{r}|\mathbf{r}_i)$ is required. To obtain $p(\mathbf{r}|\mathbf{r}_i)$, the 2D location PDFs in x and y are calculated by marginalizing equation (A1) over all angles. Assuming circular symmetric PBs, $p(\mathbf{r}|\mathbf{r}_i)$ is the product of the location PDFs in x and y:

$$p(\mathbf{r}|\mathbf{r}_i) = \frac{1}{\pi\sigma_l^2(z)}\exp\left(-\frac{(x-x_i)^2+(y-y_i)^2}{\sigma_l^2(z)}\right). \tag{A2}$$

Here, $\sigma_x^2(z) = \sigma_y^2(z) \equiv \sigma_l^2(z)$ is the spatial spread of the beam at z, whose calculation is detailed in appendix A.2.

A.2. Definition of $\boldsymbol{\Sigma}_x(z)$

The approach to estimate the components of the spatio-angular covariance matrix $\boldsymbol{\Sigma}_x(z)$, first introduced in equation (1), is reported for completeness. Considering a PB starting at location $z = z_1$ and propagating through z_2 cm of homogeneous material, the elements of the covariance matrix can be calculated using equations (A3)–(A5) (Gottschalk 2012):

$$\sigma_{\theta_l}^2(z_1, z_2) = \sigma_{\theta_l}^2(z_1) + \mathcal{A}_0(z_1, z_2). \tag{A3}$$

$$\sigma_{l\theta_l}(z_1, z_2) = \sigma_{l\theta_l}(z_1) + \sigma_{\theta_l}^2(z_1)z_2 + \mathcal{A}_1(z_1, z_2). \tag{A4}$$

$$\sigma_l^2(z_1, z_2) = \sigma_l^2(z_1) + 2\sigma_{l\theta_l}(z_1)z_2 + \sigma_{\theta_l}^2(z_1)z_2^2 + \mathcal{A}_2(z_1, z_2). \tag{A5}$$

The $\mathcal{A}_n(z_1, z_2)$, with $n \in \{0, 1, 2\}$, are pure multiple scattering contributions, and are defined as moments of the depth-dependent linear scattering power $T(z')$. For a particle of charge Z, $T(z')$ can be modelled using Gottschalk's adaptation of Highland's formula (Gottschalk *et al* 1993), with the refined constants from Lynch and Dahl (Lynch and Orin 1991):

$$\mathcal{A}_n(z_1, z_2) \equiv \frac{1}{2}\int_{z_1}^{z_2}(z_2 - z')^n T(z')\mathrm{d}z' = Z^2E_0^2\left(1 + 0.038\ln\left(\int_{z_1}^{z_2}\frac{\mathrm{d}z'}{X_0}\right)\right)^2 \times \int_{z_1}^{z_2}\frac{(z_2 - z')^n}{p^2(z')\beta^2(z')X_0}\mathrm{d}z'. \tag{A6}$$

Where $E_0 = 13.6\ MeV$, X_0 is the radiation length of the medium, and $p(z')$, $\beta(z')$ are respectively the proton momentum and velocity (relative to c) at depth z'. Equation (A6) requires a model of how protons lose energy as a function of depth. In this work, $p^2(z')\beta^2(z')$ is directly calculated using tabulated stopping power data from the PSTAR database (Berger *et al* 2005), instead of using parametric approximations (Williams 2004, Schulte *et al* 2008, Kanematsu 2009, Gottschalk 2010).

For an heterogeneous geometry, equations (A3)–(A5) are applied recursively to propagate a beam through a stack of homogeneous slabs—using the final state of $\boldsymbol{\Sigma}_x(z)$ after the first slab as the initial state for $\boldsymbol{\Sigma}_x(z)$ to the second slab, and so on. All $\sigma_l(z)$ encountered in sections 2.2.1–2.2.3 are calculated in heterogeneous geometries; details are provided in appendix B.

Appendix B. Calculating $\sigma_l(z)$ for heterogeneous geometries

To estimate $\sigma_l(z)$ for the scenarios discussed in sections 2.2.1–2.2.3, a schematized geometry for each case is presented in figure 9. Each geometry is detailed in sections B.1–B.3.

B.1. Calculation for $\mathcal{P}(r_k|r_i)$

Following figure 9, $\sigma_l(z_k)$ is obtained in two steps: propagation in air from $z_i = 0$ to the object's entrance at z_O, and propagation through z_k cm inside the object, assumed to be water-equivalent.

Considering the nomenclature introduced in section A.2, $\sigma_l(z_k)$ is obtained as follows. First, the initial state of the PB is taken as $\boldsymbol{\Sigma}_x(z_i)$, as defined in equation (1). Then, each component of $\boldsymbol{\Sigma}_x(z_i)$ is transported in air from z_i to z_O; following equations (A3) to (A5), this is achieved by calculating $\sigma_{\theta_l}^2(z_i, z_O)$, $\sigma_{l\theta_l}(z_i, z_O)$ and $\sigma_l^2(z_i, z_O)$. This set of parameters provide $\sigma_l(z_O)$, the state of the PB at z_O, which is used as an initial condition to transport the beam in water from z_O to z_k as $\sigma_l^2(z_i, z_O)$, and so on for the angular spread and covariance term.

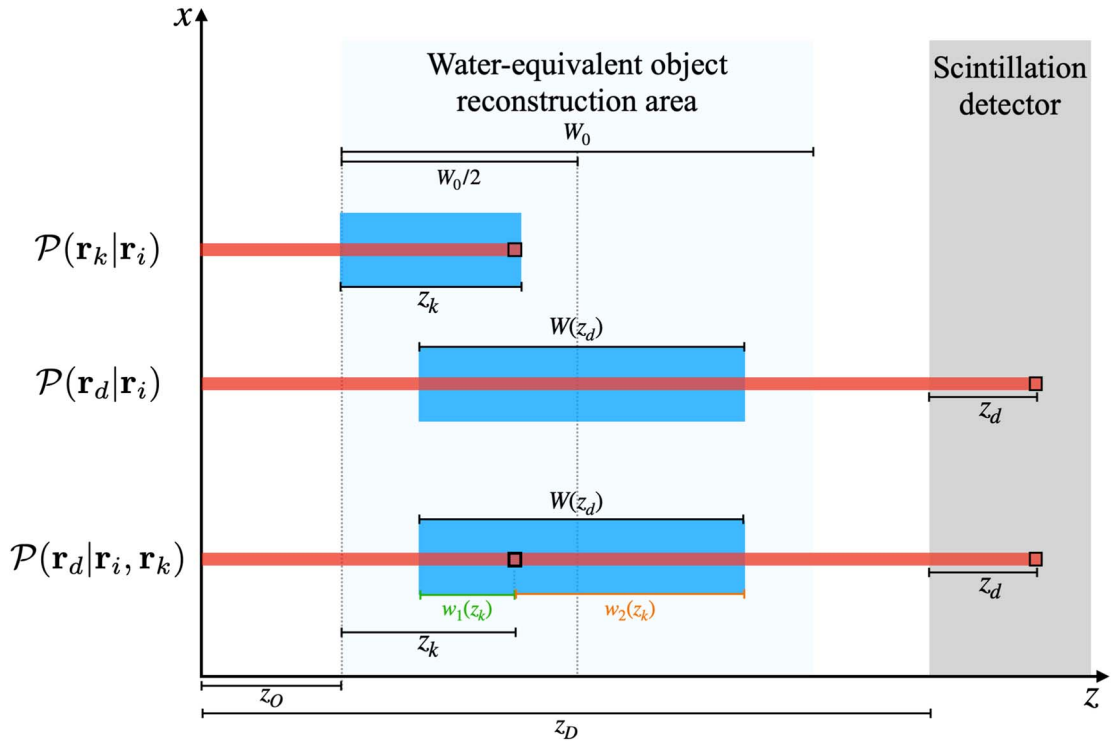

Figure 9. Proposed geometries to calculate $\sigma_l(z)$ for each likelihood term. z_O and z_D are respectively the source to object and source to detector distances. z_k and z_d are respectively depths traversed inside the object geometry and detector. The maximum WET of the object is W_0, the range of the PB in water. For probabilities involving $\mathbf{r}_d$, it is assumed that the traversed WET of the object by the PB, $W(z_d)$, is located at the centre of the reconstruction area. $w_1(z_k)$ and $w_2(z_k)$ are distances traversed within $W(z_d)$ respectively before and after a reconstruction voxel at depth z_k.

To simplify the above, the calculation of $\sigma_l(z_k)$ is summarized as calculating (1) $\sigma_l(z_i,\ z_O)$ in air and (2) $\sigma_l(z_O,\ z_k)$ in water; it is implied that all elements of the covariance matrix are calculated, and the initial state of the PB for a new step is the final state of the beam from the previous step.

B.2. Calculation for $\mathcal{P}(r_d|r_i)$

To calculate $\sigma_l(z_d)$, it is assumed that if a PB is detected at depth z_d, it is because it completed its course. From this hypothesis, one can infer the traversed WET of the object by the PB, $W(z_d)$, directly from the depth z_d at which the PB was detected; see equation (11).

While it is known that a slab of $W(z_d)$ cm of water-equivalent object is traversed, there is no information on the position of this slab between the source and the detector, as no object hull is estimated. It is approximated that the slab of water-equivalent object is centred in the middle of the reconstruction area at $z = z_O + \frac{W_0}{2}$, as illustrated in figure 9.

Let $w_\pm = \frac{W_0 \pm W(z_d)}{2}$. Then, following the simplified notation introduced in section B.1, the spread of the beam $\sigma_l(z_d)$ through the heterogeneous geometry is then obtained by recursively calculating (1) $\sigma_l(z_i,\ z_O + w_-)$ in air, (2) $\sigma_l(z_O + w_-,\ W(z_d))$ in water, (3) $\sigma_l(z_O + w_+,\ z_D - z_O - w_+)$ in air, and (4) $\sigma_l(z_D,\ z_d)$ in the detector.

B.3. Calculation for $\mathcal{P}(r_d|r_i,\ r_k)$

As introduced in section 2.2.2, the calculation of $\mathcal{P}(\mathbf{r}_d|\mathbf{r}_i,\ \mathbf{r}_k)$ involves the beam stopping at z_d, which implies crossing a WET of $W(z_d)$ in the object, as defined in equation (11). As introduced in section B.2, the location of the object slab of water equivalent thickness $W(z_d)$ with respect to the coordinate z_k is unknown without prior information on the object's hull; in other words, calculating the spread at depth z_k in the object does not necessarily involve crossing z_k cm of water. As a solution, it is also assumed that the object slab is located at the centre of the reconstruction area, which naturally fixes the WET traversed from z_O to z_k, $w_1(z_k)$, as

$$w_1(z_k) = \begin{cases} 0 & \text{if} \quad z_k < w_-; \\ z_k - w_- & \text{if} \quad z_k \in [w_-,\ w_+]; \\ W(z_d) & \text{if} \quad z_k > w_+. \end{cases} \tag{B1}$$

Similarly, the traversed depth in the object from z_k to z_D is $w_2(z_k) = W(z_d) - w_1(z_k)$. To obtain $\sigma_l^2(z_k)$ (and the other covariance matrix elements) required in equations (7), one should calculate, following the simplified notation introduced in section B.1, (1) $\sigma_l(z_i,\ z_O + z_k - w_1(z_k))$ in air, and (2)$\sigma_l(z_O + z_k - w_1(z_k),\ w_1(z_k))$ in water.

Otherwise, equations (7) also involve the calculation of $\mathcal{A}_2(z)$, which is the pure multiple scattering contribution to the spatial spread from the object voxel's location z_k to an arbitrary depth z inside the detector. This is obtained by recursively applying equation (A6) throughout the geometry.

Appendix C. Dose considerations

Proton radiographs were initially acquired at the lowest achievable dose of 0.003 MU/spot. The dose in cGy was measured by collecting the charge in a Farmer Ionization Chamber (PTW30010) within a 15 cm^3 acrylic cube setup. The chamber was placed at a depth of 5 cm and dose measured at the two energies and various beam spacings used in this study. Values are reported in table 2.

Due to the low frame rate of the CMOS camera, some pencil beams were not captured at 0.003 MU/spot. To address this limitation, we increased the dose by a factor of approximately 100 such that the time to deliver each pencil beam was long enough to ensure that all pencil beams could be captured. The dose values are also reported in the last row of table 2.

The robustness of the peak finding algorithm (section 2.3.2) to noisier measurements (lower dose) was evaluated by acquiring single pencil beams at the two doses (dose used for radiographs against dose at 0.003 MU/spot) and comparing the extracted values of z_d. As z_d was found to not vary by more than 3 pixels, the proposed method is assumed to be robust in the presence of noise. Therefore, the high dose should therefore be seen as the consequence of the limited acquisition speed of the camera, and the lower doses reported in table 2 are more representative of the currently achievable doses for integrated mode proton radiographs.

Table 2. Reported dose of the treatment plans used to produce the proton radiographs as a function of energy and beam spacing.

	135.6 MeV				**189 MeV**		
Beam spacing (mm)	2	3	4	5	2	3	4
Dose at 0.003 MU/spot (cGy)	6.2	2.8	1.5	1.0	5.7	2.5	1.4
Dose used for radiographs (cGy)	515.2	257.2	128.9	82.4	475.9	226.8	238.4

ORCID iDs

Mikaël Simard https://orcid.org/0000-0003-0610-6319
Ryan Fullarton https://orcid.org/0000-0001-7817-1596
Sam Beddar https://orcid.org/0000-0001-5825-110X

References

Agostinelli S *et al* 2003 Geant4âa simulation toolkits *Nucl. Instrum. Methods Phys. Res.* A **506** 250–303
Alsanea F, Darne C, Hojo Y and Beddar S 2019 A novel imaging scheme for optical cameras used in a quality assurance detector for discrete spot scanning proton beam systems *Nucl. Instrum. Methods Phys. Res.* A **939** 16–21
Berger M J, Coursey J S, Zucker M A and Chang J 2005 Stopping-power & range tables for electrons, protons, and helium ions *NIST standard reference database 124* https://doi.org/10.18434/T4NC7P
Collins-Fekete C-A, Volz L, Portillo S, Beaulieu L and Seco J 2017 A theoretical framework to predict the most likely ion path in particle imaging *Phys. Med. Biol.* **62** 1777
Darne C, Alsanea F, Robertson D, Guan F, Pan T, Grosshans D and Beddar S 2019 A proton imaging system using a volumetric liquid scintillator: a preliminary study *Biomed. Phys. Eng. Express* **5** 045032
Darne C D, Alsanea F, Robertson D G, Sahoo N and Beddar S 2017 Performance characterization of a 3D liquid scintillation detector for discrete spot scanning proton beam systems *Phys. Med. Biol.* **62** 5652
Darne C D, Robertson D G, Alsanea F, Collins-Fekete C-A and Beddar S 2022 A novel proton-integrating radiography system design using a monolithic scintillator detector: Experimental studies *Nucl. Instrum. Methods Phys. Res.* A **1027** 166077
Dedes G *et al* 2022 Comparative accuracy and resolution assessment of two prototype proton computed tomography scanners *Med. Phys.* **49** 4671–81
Deffet S, Farace P and Macq B 2020 Sparse deconvolution of proton radiography data to estimate water equivalent thickness maps *Med. Phys.* **47** 509–17
Du P, Kibbe A and Lin S M 2006 Improved peak detection in mass spectrum by incorporating continuous wavelet transform-based pattern matching *Bioinformatics* **22** 2059–65
Evans J D *et al* 2020 The importance of verification ct-qa scans in patients treated with impt for head and neck cancers *Int. J. Part. Ther.* **7** 41–53
Eyges L 1948 Multiple scattering with energy loss *Phys. Rev.* **74** 1534
Farace P, Righetto R and Meijers A 2016 Pencil beam proton radiography using a multilayer ionization chamber *Phys. Med. Biol.* **61** 4078
Fermi E 1940 The ionization loss of energy in gases and in condensed materials *Phys. Rev.* **57** 485
Fujita H, Tsai D-Y, Itoh T, Doi K, Morishita J, Ueda K and Ohtsuka A 1992 A simple method for determining the modulation transfer function in digital radiography *IEEE Trans. Med. Imaging* **11** 34–9
Fukumitsu N *et al* 2014 Dose distribution resulting from changes in aeration of nasal cavity or paranasal sinus cancer in the proton therapy *Radiother. Oncol.* **113** 72–6
Gottschalk B 2010 On the scattering power of radiotherapy protons *Med. Phys.* **37** 352–67
Gottschalk B 2012 Techniques of proton radiotherapy: transport theory arXiv:1204.4470
Gottschalk B, Koehler A M, Schneider R J, Sisterson J M and Wagner M S 1993 Multiple coulomb scattering of 160 mev protons *Nucl. Instrum. Methods Phys. Res.*B **74** 467–90
Ibbott G S 1985 Radiation dosimetry: electron beams with energies between 1 and 50 mev *ICRU Report* 35
Jette D, Pagnamenta A, Lanzl L H and Rozenfeld M 1983 The application of multiple scattering theory to therapeutic electron dosimetry *Med. Phys.* **10** 141–6
Johnson R 2017 Review of medical radiography and tomography with proton beams *Rep. Prog. Phys.* **81** 016701
Kanematsu N 2009 Semi-empirical formulation of multiple scattering for the gaussian beam model of heavy charged particles stopping in tissue-like matter *Phys. Med. Biol.* **54** N67
Krah N, De Marzi L, Patriarca A, Pittá G and Rinaldi I 2018a Proton radiography with a commercial range telescope detector using dedicated post processing methods *Phys. Med. Biol.* **63** 205016
Krah N, Khellaf F, Létang J M, Rit S and Rinaldi I 2018b A comprehensive theoretical comparison of proton imaging set-ups in terms of spatial resolution *Phys. Med. Biol.* **63** 135013
Langner U W, Eley J G, Dong L and Langen K 2017 Comparison of multi-institutional varian probeam pencil beam scanning proton beam commissioning data *J. Appl. Clin. Med. Phys.* **18** 96–107
Lynch G R and Dahl O I 1991 Approximations to multiple coulomb scattering *Nucl. Instrum. Methods Phys. Res.*B **58** 6–10
Magallanes L, Meyer S, Gianoli C, Kopp B, Voss B, Jäkel O, Brons S, Gordon J and Parodi K 2019 Upgrading an integrating carbon-ion transmission imaging system with active scanning beam delivery toward low dose ion imaging *IEEE Trans. Radiat. Plasma Med. Sci.* **4** 262–8
Meijers A, Seller Oria C, Free J, Langendijk J, Knopf A and Both S 2021 First report on an in vivo range probing quality control procedure for scanned proton beam therapy in head and neck cancer patients *Med. Phys.* **48** 1372–80
Oria C, Free J, Marmitt G, Knäusl B, Brandenburg S, Knopf A, Meijers A, Langendijk J and Both S 2023 Flat panel proton radiography with a patient specific imaging field for accurate wepl assessment *Med. Phys.* **50** 1756-65
Paganetti H 2012 Range uncertainties in proton therapy and the role of monte carlo simulations *Phys. Med. Biol.* **57** R99
Parodi K 2020 Latest developments in in-vivo imaging for proton therapy *Br. J. Radiol.* **93** 20190787
Rescigno R, Bopp C, Rousseau M and Brasse D 2015 A pencil beam approach to proton computed tomography *Med. Phys.* **42** 6610–24
Rinaldi I, Brons S, Jäkel O, Voss B and Parodi K 2014 Experimental investigations on carbon ion scanning radiography using a range telescope *Phys. Med. Biol.* **59** 3041
Rit S, Dedes G, Freud N, Sarrut D and Létang J M 2013 Filtered backprojection proton ct reconstruction along most likely paths *Med. Phys.* **40** 031103
Robertson D, Hui C, Archambault L, Mohan R and Beddar S 2013 Optical artefact characterization and correction in volumetric scintillation dosimetry *Phys. Med. Biol.* **59** 23
Sabbas A M, Jette D, Rozenfeld M, Pagnamenta A and Lanzl L H 1987 Collimated electron beams and their associated penumbra widths *Med. Phys.* **14** 996–1006

Safai S, Bortfeld T and Engelsman M 2008 Comparison between the lateral penumbra of a collimated double-scattered beam and uncollimated scanning beam in proton radiotherapy *Phys. Med. Biol.* **53** 1729
Schaffner B and Pedroni E 1998 The precision of proton range calculations in proton radiotherapy treatment planning: experimental verification of the relation between ct-hu and proton stopping power *Phys. Med. Biol.* **43** 1579
Schneider U and Pedroni E 1995 Proton radiography as a tool for quality control in proton therapy *Med. Phys.* **22** 353–63
Schneider U, Pemler P, Besserer J, Pedroni E, Lomax A and Kaser-Hotz B 2005 Patient specific optimization of the relation between CT-Hounsfield units and proton stopping power with proton radiography *Med. Phys.* **32** 195–9
Schnürle K *et al* 2023 Development of integration mode proton imaging with a single cmos detector for a small animal irradiation platform *Front. Phys.* **10**
Schulte R W, Penfold S N, Tafas J T and Schubert K E 2008 A maximum likelihood proton path formalism for application in proton computed tomography *Med. Phys.* **35** 4849–56
Sechopoulos I, Rogers D W, Bazalova-Carter M, Bolch W E, Heath E C, McNitt-Gray M F, Sempau J and Williamson J F 2018 Records: improved reporting of monte carlo radiation transport studies: report of the aapm research committee task group 268 *Med. Phys.* **45** e1–5
Segars W P, Sturgeon G, Mendonca S, Grimes J and Tsui B M 2010 4D XCAT phantom for multimodality imaging research *Med. Phys.* **37** 4902–15
Steinsberger T, Donetti M, Lis M, Volz L, Wolf M, Durante M and Graeff C 2022 Experimental validation of an online adaptive 4D-optimized particle radiotherapy approach to treat irregularly moving tumors *Int. J. Radiat. Oncol.* Biol.* Phys.* **115** 1257–68
Tanaka S, Nishio T, Matsushita K, Tsuneda M, Kabuki S and Uesaka M 2016 Development of proton CT imaging system using plastic scintillator and CCD camera *Phys. Med. Biol.* **61** 4156
Tanaka S, Nishio T, Tsuneda M, Matsushita K, Kabuki S and Uesaka M 2018 Improved proton ct imaging using a bismuth germanium oxide scintillator *Phys. Med. Biol.* **63** 035030
Tendler I, Robertson D, Darne C, Panthi R, Alsanea F, Collins-Fekete C-A and Beddar S 2021 Image quality evaluation of projection-and depth dose-based approaches to integrating proton radiography using a monolithic scintillator detector *Phys. Med. Biol.* **66** 144001
Testa M, Verburg J, Rose M, Min C, Tang S, Bentefour E, Paganetti H and Lu H-M 2013 Proton radiography and proton computed tomography based on time-resolved dose measurements *Phys. Med. Biol.* **58** 8215
Van der Heyden B, Cohilis M, Souris K, de Freitas Nascimento L and Sterpin E 2021 Artificial intelligence supported single detector multi-energy proton radiography system *Phys. Med. Biol.* **66** 105001
Volz L, Collins-Fekete C-A, Sølie J R and Seco J 2020 Theoretical considerations on the spatial resolution limit of single-event particle radiography *Biomed. Phys. Eng. Express* **6** 055002
Williams D C 2004 The most likely path of an energetic charged particle through a uniform medium *Phys. Med. Biol.* **49** 2899
Wu R Y *et al* 2017 Intensity-modulated proton therapy adaptive planning for patients with oropharyngeal cancer *Int. J. Part. Ther.* **4** 26–34
Yang M, Zhu X, Park P, Titt U, Mohan R, Virshup G, Clayton J and Dong L 2012 Comprehensive analysis of proton range uncertainties related to patient stopping-power-ratio estimation using the stoichiometric calibration *Phys. Med. Biol.* **57** 4095
Zygmanski P, Gall K, Rabin M and Rosenthal S 2000 The measurement of proton stopping power using proton-cone-beam computed tomography *Phys. Med. Biol.* **45** 511